Simulations of flow around a simplified train model with a drag reducing device

Conference on Modelling Fluid Flow (CMFF'12)
The 15th International Conference on Fluid Flow Technologies
Budapest, Hungary, September 4-7, 2012

Simulations of Flow Around a Simplified Train Model with a Drag Reducding Device using Partially Averaged Navier-Stokes

Jan ÖSTH[1], Siniša KRAJNOVIĆ[2]

[1] Corresponding Author. Division of Fluid Dynamics. Department of Applied Mechanics, Chalmers University of Technology. Hörsalsvägen 7A, SE-412 96 Göteborg, Sweden. Tel.: +46 31 772 13 90, Fax: +46 31 18 09 76, E-mail: ojan@chalmers.se
[2] Division of Fluid Dynamics. Department of Applied Mechanics, Chalmers University of Technology. www.tfd.chalmers.se/~sinisa, E-mail: sinisa@chalmers.se

ABSTRACT

Partially Averaged Navier Stokes is used to simulate the flow around a simple train model. The train model has previously been studied in wind tunnel experiments [1] and has a length to height/width ratio of 7:1. The Reynolds number based on the height of the train model is $0.37 \cdot 10^6$. For this Reynolds number, the flow separates from the curved leading edges on the front then attaches again on the roof and sides forming a boundary layer there before separating in the wake. The first case is of the natural flow around the train model where direct comparison to experimental data of drag coefficient and pressure coefficient are made. In the second case an open cavity is placed on the base of the train model with the aim of reducing the overall drag on the model. The results show that the drag for model with the cavity is reduced by some 10% compared to the drag of the natural case. The agreement to experimental data for the natural case is not perfect but the general features in the flow field are simulated correctly.

Train aerodynamics, PANS, Drag reduction, CFD

NOMENCLATURE

C_D	$[-]$	Drag force coefficient
C_p	$[-]$	Pressure coefficient
F_x	$[N]$	Force in stream wise direction
F_y	$[N]$	Force in span wise direction
f_k	$[-]$	Ratio of unresolved kinetic energy to resolved
f_ϵ	$[-]$	Ratio of unresolved dissipation to resolved
k_u	$[m^2/s^2]$	Unresolved kinetic energy
p_F	$[Pa]$	Filtered pressure
u_i	$[m/s]$	Filtered velocities
ζ_u	$[-]$	Velocity scale ratio
ϵ_u	$[m^2/s^3]$	Unresolved dissipation
ρ	$[kg/m^3]$	Density
ν	$[kg/sm]$	Molecular viscocity
ν_u	$[kg/sm]$	Viscosity of the unresolved scales

HST	High Speed Train
RT	Regional Train
PANS	Partially Averaged Navier-Stokes

1. INTRODUCTION

Aerodynamic issues concerning railway systems are numerous. Aerodynamic noise generated by the train has a negative influence on the environment around the railway system and on the passengers inside the train. Pressure variations in tunnels increase the drag of the train significantly in comparison to open air and can cause considerable ear discomfort for passengers in the train and riding discomfort due to large dynamic oscillation of the train. Pressure waves radiate to the environment from the tunnel exit. The increased driving resistance inside tunnels increase the mechanical stress on the train. The slip stream (a very strong shear layer) formed around the moving train can cause serious accidents to persons or material located on platforms when trains pass by. Cross-winds can cause very serious accidents such as derailment [2]. The aerodynamic drag induced on the train affects the economics of the railway system considerably and limits the maximum speed. High speed trains (HST) are in general shaped in a very good way in regard to minimizing the aerodynamic drag. However, still it is responsible for the consumption of some 40-50% of the total energy put into the railway system during traction [3] for a typical HST. For regional type (RT) of trains, the aerodynamic drag contributes less to the total energy consumption due to the typical lower operational speeds. In general regional trains have a worse shape from an aerodynamic drag minimizing point of view compared to high speed trains. The

contribution to the total aerodynamic drag on a train comes from different areas of the train: skin friction drag along the train body, pantographs and other protruding objects, inter-carriage gaps, brakes, boogies and the pressure difference between the head and the tail of the train, the last one being dominating for RT trains [3].

One way to increase the base pressure and thereby reduce the aerodynamic drag on trains having a square back such as the Bombardier Contessa/X31 train used in southern Sweden could be to place plates forming a cavity on the aft of the train. Such devices has proven to be able to reduce the drag on simplified ground vehicle models in wind tunnel experiments and numerical simulations [4, 5] as well as on real tractor-trailers during over-the-road tests [6, 7].

The work reported in the present paper aims at reducing the drag on a simplified train model by attaching an aft cavity on the base of the train. The investigation method used in the present work is unsteady numerical simulations using the recently proposed hybrid turbulence modeling method Partially Averaged Navier Stokes (PANS). The train model has previously been investigated in wind tunnel experiments by Sakuma & Ido [1]. Two cases are simulated: the natural case and the cavity case. For the natural case, direct comparison with experimental data is possible. For the aft cavity case however, no direct experimental data are available. The outline of the paper is as follows: in Section 2 the train model for the two cases and the reference experiments are described. In Section 3 the PANS equations are presented. In Section 4 the numerical details of the simulations are described. Then follows the results from the simulations in Section 5.1 and in the last Section the results are discussed and the paper is concluded.

2. THE TRAIN MODEL AND REFERENCE EXPERIMENT

The train model used in the numerical investigation in the present paper is taken from the wind tunnel experiments reported in [1] where the large-scale wind tunnel [8] at Railway Technical Research Institute (RTRI) was used . The train model, presented in Fig. 1, is a prismatic bluff body with the height H and width $W = H = 0.56\,m$. The length of the bluff body is $7H$ which thus makes it resemble some RT trains better than other bluff bodies with smaller length-to-height ratio reported in the literature (e.g. [9]). The aim of the extensive experimental study reported in [1] was to investigate how the separation from the leading front edges of the bluff body was affected by different roundings of the front edges for a Reynolds number of $1.9 \cdot 10^6$ and $0.37 \cdot 10^6$ based on the width of the train. The former Reynolds number corresponds roughly to one third of that of a real regional train travelling at 120 km/h.

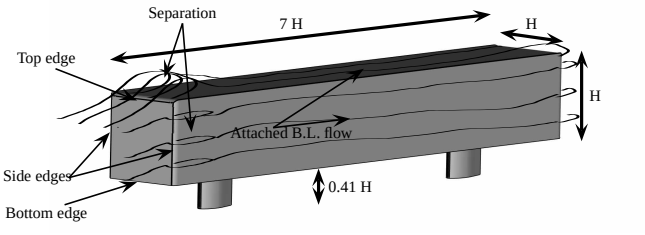

Figure 1. Schematic drawing of the train model and the flow around it at the low Reynoldsnumber $Re_H = 0.37 \cdot 10^6$.

One of the configurations from [1] is choosen for the simulations presented in the present paper. In the choosen configuration the leading top and side edges on the front are rounded using an elliptic profile (see Fig 2). The major axis in the ellipse has length $0.07H$ and the minor axis has length $0.04H$. The bottom edge is not rounded at all and is thus sharp. The model was placed on two egg-shaped supports in the wind tunnel and the model is lifted 0.41 H above the ground. The top and side edges on the rear end of the bluff body are rounded with a circular radius of 0.107H while the bottom edge here is sharp.

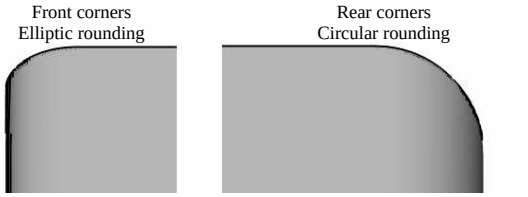

Figure 2. The front and rear corners of the train model, respectively.

For the choosen configuration from [1] which make up the natural case in the present study and $Re_H = 0.37 \cdot 10^6$ the flow separates from the leading edges on the front of the bluff body (see Fig. 1). After a distance of approximately $\approx H$, the flow re-attaches on the top and the sides of the body and an attached boundary layer develops along the body before the flow separates in the wake once again. There are thus three major very difficult flow situations to simulate in this case. If not the separation on the front leading edges are simulated correctly, the boundary layer will not be simulated correctly and that will make it impossible to simulate the separation in the wake in a correct manner. The reported drag coefficient of the bluff body at $Re_H = 0.39 \cdot 10^6$ in the experimental study is $C_D^{low} = 0.86$ and for $Re_H = 1.9 \cdot 10^6$ it is $C_D^{high} = 0.41$ [1]. This significantly smaller drag coefficient for the high Reynolds number is because the flow in that case does not separate from the

leading front edges and thus stays attached all the way to the rear of the bluff body.

2.1. *Cavity case: attached open cavity on the base of the train model*

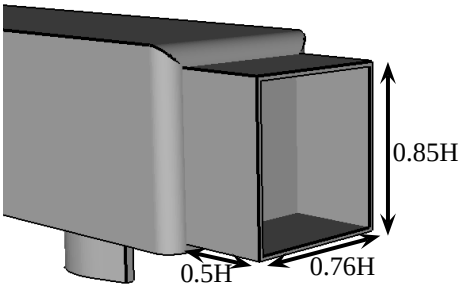

Figure 3. The flaps attached on the base of the train model.

The cavity placed on the aft on the train model is depicted in Fig. 3. The length of the cavity is 0.5 H which corresponds to the length that was found to be optimal in the previously mentioned studies [6, 7] where a cavity was attached on the base of a real tractor-trailer. The inset of the cavity from the bottom edge is 0.06 H corresponding to the optimum value from the studies. The inset from the side and top edges are choosen such that the plates are placed on the end of the curvature on the edges.

3. PANS GOVERNING EQUATIONS

Two crucial parameters in PANS are $f_k = k_u/k$ and $f_\epsilon = \epsilon_u/\epsilon$. The former is the ratio of unresolved kinetic energy to the resolved kinetic energy. The latter is the ratio of unresolved dissipation to the total dissipation in the flow. For the formal derivation and motivation of the PANS method the reader is referred to [10]. Herein, the equations are simply stated. The governing flow equations are the incompressible, partially filtered Navier-Stokes Equations (NSE):

$$\frac{\partial u_i}{\partial x_i} = 0 \tag{1}$$

$$\frac{\partial u_i}{\partial t} + u_j\frac{\partial u_i}{\partial x_j} = -\frac{1}{\rho}\frac{\partial p_F}{\partial x_i} + \frac{\partial}{\partial x_j}(\nu\frac{\partial u_i}{\partial x_j} - \tau(u_i,u_j)) \tag{2}$$

In Eqs. (1) and (2) $u_i = \langle v_i\rangle$ are the partially filtered velocities. v_i are the unfiltered velocities containing all spatial and temporal scales in the flow and $\langle\cdot\rangle$ denotes filtering by an arbitrary filter (in time and space) fulfilling the requirements for averaging invariance [11]. $p_F = \langle p\rangle$ is the partially filtered pressure. $\tau(v_i,v_j) = \langle v_iv_j\rangle - \langle v_i\rangle\langle v_j\rangle$ is the sub-filter scale (SFS) stress which is modelled by the turbulent-viscosity (Boussinesq) assumption:

$$\tau(v_i,v_j) - \frac{2}{3}k_u\delta_{ij} = -2\nu_u S_{ij} \tag{3}$$

In Eq. (3) $k_u = \frac{1}{2}\tau(v_i,v_i)$ is the kinetic energy of the unresolved motion (sub-filter scales) in the flow. $S_{ij} = \frac{1}{2}(\partial u_i/\partial x_j + \partial u_j/\partial x_i)$ is the rate-of-strain tensor of the resolved motion (the partially filtered velocities). ν_u is the eddy viscosity of the unresolved motion. The simulations in this work employs the PANS $k-\epsilon-\zeta-f$ model [12] which previously has been used to simulate the complex unsteady flow around a rudimentary landing gear and for active flow control [13, 14]. ν_u is thus modelled as:

$$\nu_u = C_\mu\zeta_u\frac{k_u^2}{\epsilon_u} \tag{4}$$

Here, $\zeta_u = \overline{v_u^2}/k_u$ is the velocity scale ratio of the unresolved velocity scales $\overline{v_u^2}$ and k_u. $\overline{v_u^2}$ refers to the normal fluctuating component of the velocity field to any no-slip boundary, see Ref. [15] for further details and argumentation for the concept of introducing the normal velocity scale. ϵ_u is the dissipation of the unresolved scales. The four model equations for the quantities in Eq. (4) are:

$$\frac{\partial k_u}{\partial t} + u_j\frac{\partial k_u}{\partial x_j} = (P_u - \epsilon_u) + \frac{\partial}{\partial x_j}[(\nu + \frac{\nu_u}{\sigma_{ku}})\frac{\partial k_u}{\partial x_j}] \tag{5}$$

In Eq. (5) $P_u = -\tau(v_i,v_j)\frac{\partial u_i}{\partial x_j}$ is the production of unresolved kinetic energy which is closed by the relation in Eq. 3.

$$\frac{\partial \epsilon_u}{\partial t} + u_j\frac{\partial \epsilon_u}{\partial x_j} = C_{\epsilon1}P_u\frac{\epsilon_u}{k_u} - C^*_{\epsilon2}\frac{\epsilon_u^2}{k_u} + \frac{\partial}{\partial x_j}(\frac{\nu_u}{\sigma_{\epsilon_u}}\frac{\partial \epsilon_u}{\partial x_j}) \tag{6}$$

$$C^*_{\epsilon2} = C_{\epsilon1} + \frac{f_k}{f_\epsilon}(C_{\epsilon2} - C_{\epsilon1}) \tag{7}$$

$$\sigma_{ku,\epsilon u} = \sigma_{k,\epsilon}\frac{f_k^2}{f_\epsilon} \tag{8}$$

$$C_{\epsilon1} = 1.4(1 + 0.045/\sqrt{\zeta_u}) \tag{9}$$

$$\frac{\partial \zeta_u}{\partial t} + u_j\frac{\partial \zeta_u}{\partial x_j} = f_u - \frac{\zeta_u}{k_u}P_u + \frac{\zeta_u}{k_u}\epsilon_u(1-f_k) + \frac{\partial}{\partial x_j}(\frac{\nu_u}{\sigma_{\zeta u}}\frac{\partial \zeta_u}{\partial x_j}) \tag{10}$$

$$L_u^2\nabla^2 f_u - f_u = \frac{1}{T_u}(c_1 + c_2\frac{P_u}{\epsilon_u})(\zeta_u - \frac{2}{3}) \tag{11}$$

The integral length and times scales of the unresolved scales L_u and T_u in Eq. 11 are computed using the unresolved kinetic energy. The parameter f_k is choosen as:

$$f_k(\mathbf{x}) = \frac{1}{\sqrt{C_\mu}}(\frac{\Delta}{\Lambda})^{2/3} \tag{12}$$

Where Δ is the geometric-average grid cell dimension, thus $\Delta = (\Delta x\cdot\Delta y\cdot\Delta z)^{1/3}$ and Λ is the Taylor scale of turbulence. The Taylor scale of turbulence Λ is computed using the resolved and unresolved kinetic energy and dissipation, $\Lambda = (k_u +$

$k_{res})^{1.5}/\epsilon$. f_k is computed in every cell at the end of each timestep. The computed values are then used as fixed values during the next timestep. The values of the constants in the model equations are:

$$C_\mu = 0.22;\ C_{\epsilon 2} = 1.9 \quad (13)$$

$$c_1 = 0.4;\ c_2 = 0.65;\ \sigma_k = 1; \quad (14)$$

$$\sigma_\epsilon = 1.3;\ \sigma_{\zeta_u} = 1.2 \quad (15)$$

4. Numerical set-up

4.1. Numerical method

Equations (1), (2), (5), (6), (10) and (11) are discretized using a commercial finite volume solver, AVL Fire v2010.1 ([16]). The discretization is done using a collocated grid arrangement. The convective fluxes in the momentum equations are approximated by a bounded upwind scheme of second order accurancy. The convective fluxes in the model equations are approximated by an unbounded upwind scheme of second order accurancy. The time marching procedure is done using the implicit second-order accurate three-time level scheme. The pressure is determined by the SIMPLE algorithm ([17]).

4.2. Computational grid

One computational grid is used for each of the cases (natural and cavity). The grids contain only hexa-hedral elements and are constructed with the hexa-blocking method in the grid-generator software Ansys ICEM CFD. The grid for the natural case contains 12 million cells and for the controlled case the grid contrains 14.5 million cells. The grids for the two cases are identical except the necessary difference at the base of the train model where the cavity is attached in the cavity case. The computational grid on the front of the train model is shown in Fig. 4. The size of the wall-adjacent cells in the normal direction from the wall on the train model in the grids is $\Delta n_1 = 0.000045$ H.

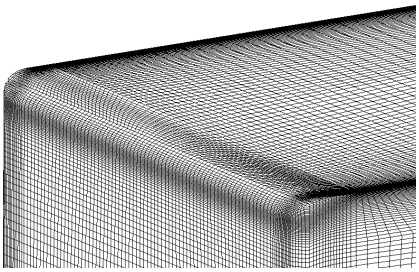

Figure 4. The grid on the front of the train model.

4.3. Computational domain and boundary conditions

The computational domain is presented in Fig. 5. Figure 5a shows the computational domain from the side. The total length of the domain is $35H$. The distances of $8H$ from the inlet to the bluff body and $20H$ after the bluff body are the same lengths as have been used in a number of similar type of unsteady numerical investigations in vehicle aerodynamics [18, 19, 20, 21]. On the inlet, a uniform velocity of $U_\infty = 10\,m/s$ in the x-direction is set. The values of k_u and ϵ_u on the inlet is set such that the ratio of the viscosity of the unresolved scales to the kinematic molecular viscosity is $\nu_u/\nu = 0.3$. On the ground plane the no-slip condition is used together with the velocity component in the x-direction equal to U_∞. This is done in order to precent developement of the boundary layer on the ground plane since in the reference experiments ([1]), the boundary layer was removed by using suction in front of the train.

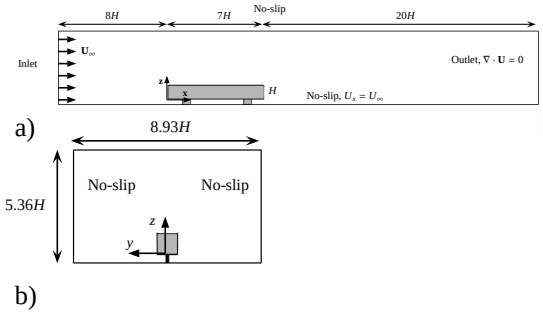

Figure 5. The wind tunnel used in the present numerical investigation. a) side view, b) front view.

The homogeneous Neumann boundary condition is applied on the outlet. On the lateral side and roof the no-slip condition is used. A front view of the computational domain is shown in the bottom figure in Fig. 5. The dimensions of the cross-section corresponds to that of the wind tunnel used in the reference experiments. The blocking ratio is approximately 2%.

4.4. Numerical accurancy: spatial and temporal resolution

The obtained spatial resolution in the simulation is presented in Table (1).

Table 1. Obtained spatial resolution in the simulations. Part I refers to the first 1/3 part of the train, Part II to the middle part of the train and Part III to the last part of the train, respectively.

		$n^+ = nu^*/\nu$	$s^+ = \Delta s u^*/\nu$	$x^+ = \Delta x u^*/\nu$
Part I	Mean	0.15	-	-
	Maximum	0.7	100	120
Part II	Mean	0.22	-	-
	Maximum	0.55	140	180
Part III	Mean	0.46	-	-
	Maximum	0.65	300	370

The time step in the simulation was choosen to 0.00015 s in physical time and in convective time units $\Delta t^* = \Delta t U_\infty / L = 0.00038$, where L is the length of the train model. This time step kept the CFL number below unity in all of the cells in the mesh except in a small volume on the curved surface on the front part of the train model where the maximum CFL number reached 2. The simulations were first run for 20 000 time steps in order to let the flow initialize. This corresponds to a fluid particle travelling through the wind tunnel 1.5 times (8 convective time units). After the initial simulation time, the time averaging of the flow properties was started. The averaging in both simulations was done during 50 000 time steps corresponding to 20 convective time units $t^* = tU_\infty / L$.

5. RESULTS

In this section some results from the simulations are presented.

5.1. Pressure coefficient - comparison with experimental data for natural case

The pressure coefficient defined as: $C_p = (p_F - p_\infty)/0.5\rho U_\infty$ is presented along a line for the natural case in Fig. 6. The pressure in the simulation follows that in the experiments. However, in the region of separated flow on the roof the negative pressure seems to be underestimate in the simulation compared to in the experiments.

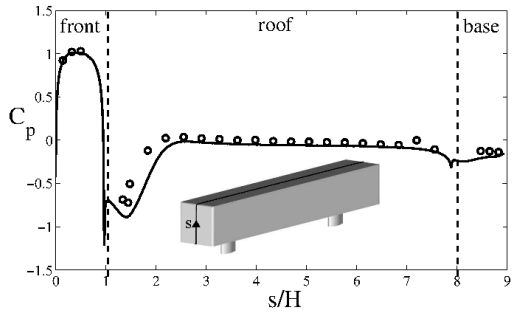

Figure 6. Pressure coefficient along a line *s* starting at origo along the mid plane of the train model for the natural case.

5.2. Global quantities

The time-averaged drag forces from the simulations are presented in Table (2). For the natural case, the drag coefficient is underestimated compared to the experiments by some 10%. The drag coefficient for the cavity case is reduced by some 10% compared to the natural case simulation. The friction part of the drag force was found to be 4% in both cases. The drag coefficient is defined as follows:

$$F_x = \frac{1}{2} C_D \rho U_\infty^2 A_x \tag{16}$$

where ρ is the density of air at 20° and $A_x = \mathrm{H}^2$.

Table 2. Time-averaged aerodynamic forces on the train model. See text for the definition of the drag coefficient.

Aerodynamic coefficients	C_D
Experiment	0.86
Natural	0.78
Controlled	0.70

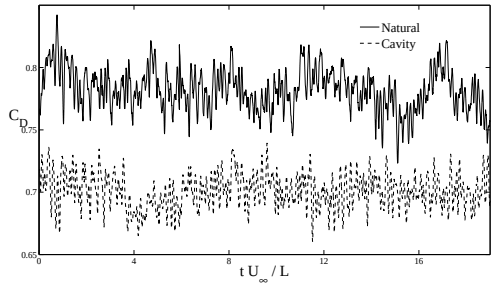

Figure 7. Time-signals of the drag forces for the natural and controlled case.

Time-signals of the drag forces are presented in Fig. 7. The size of the fluctuations in the signal is in the same order for the two cases. The root-mean square value of the drag signal for the natural case is 0.017 and for the cavity case 0.014.

5.3. Streamlines of the time-averaged flow

Stream lines of the time-averaged velocity field are presented in Figs. 8 and 9. Figure 8 shows streamlines around the first half of the train model for the two cases. The separation from the leading edges is denoted V_F in the figure. In Fig. 9 the streamlines around the second half of the model are shown. The vortex in the wake is denoted V_W. For the natural case V_W extends a distance H in the streamwise direction from the base, while for the cavity case the length of V_W is 1.5 H.

Streamlines from a top view are shown in a plane cutting the train model at $z = 0.5H$ are shown in Figs. 10 and 11.

In the cavity, an assymmetry is seen in the time-averaged flow field (see Fig. 11 b). This indicates that the flow field has not been averaged for a sufficiently long time to average the low frequency motion of the fluid inside the cavity.

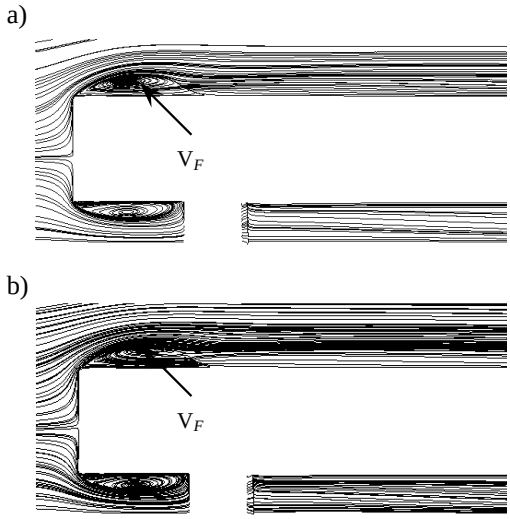

Figure 8. Streamlines of the time-averaged velocity field around the first half of the train model. a) natural case. b) cavity case. Flow is from left to right.

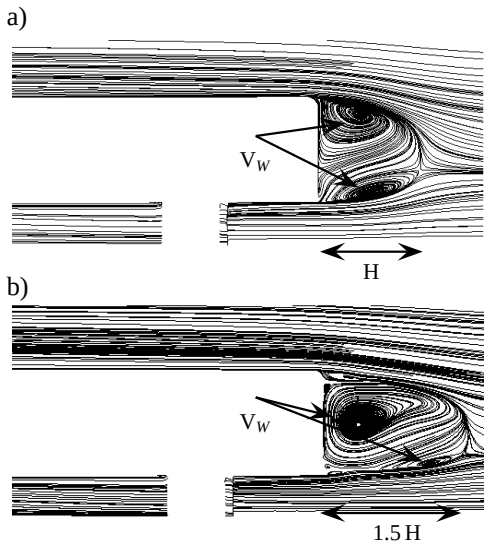

Figure 9. Streamlines of the time-averaged velocity field around the second half of the train model. a) natural case. b) cavity case.

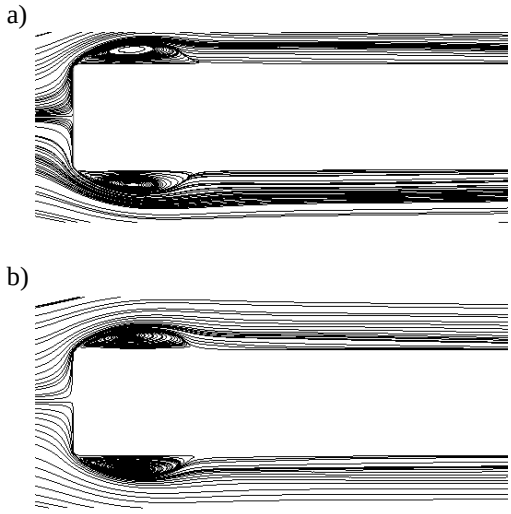

Figure 10. Streamlines of the time-averaged velocity field around the first half of the train model. a) natural case. b) cavity case.

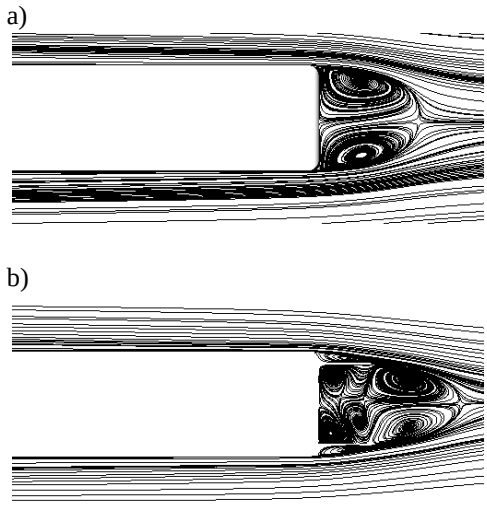

Figure 11. Streamlines of the time-averaged velocity field around the second half of the train model. a) natural case. b) cavity case. View is from above.

5.4. Pressure coefficient in the wake

The pressure coefficient is shown for the two cases in a cut in the wake behind the train model in Fig. 12. For the natural flow, the value of the pressure coefficient behind the train reaches down to −0.34. For the cavity case on the other hand, the pressure is more evenly distributed in the cavity and the value inside the cavity of the pressure coefficient is −0.08. Around the edges on the outside of the cavity the pressure coefficient is lower.

In Fig. 13 the pressure coefficient on the base face of the train model is shown for the two cases. For the natural case, the pressure is lower on the upper part of the face. For the cavity case the pressure is more evenly spread out inside the cavity. The pressure is increased on the latter case compared to the natural case in correspondence to the decreased value of the drag coefficient for the cavity case.

6. SUMMARY

In this work two simulations of the flow around a train model have been reported. The flow around the train model has previously been investigated by experiments in wind tunnel. The simulation method employed was the Partially Averaged Navier-Stokes method which is a hybrid method for turbulence modelling. The train model is a prismatic bluff body with rounded edges on the front as well as on the aft. The Reynolds number in the investigation

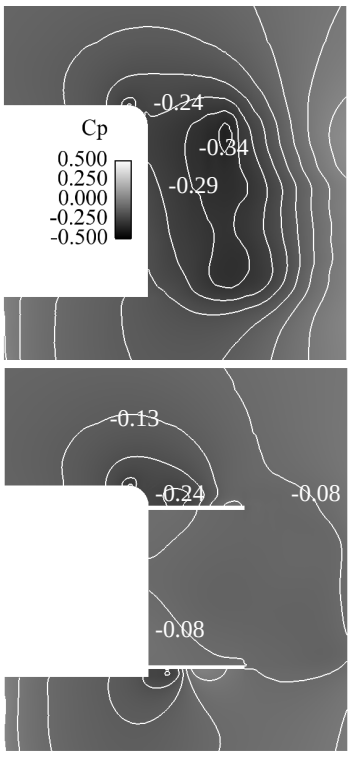

Figure 12. Pressure coefficient in the wake. a) natural case. b) cavity case. Side view.

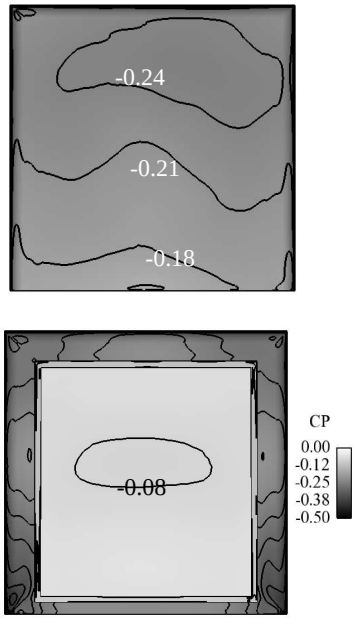

Figure 13. Pressure coefficient on the base of the train model. a) natural case. b) cavity case.

based on the height of the model was $Re_H = 0.37 \cdot 10^6$. In the experiments, for this Reynolds number, the flow separates from the curved leading edges. This separation of the flow was predicted in the simulations as well. Comparison to experimental data for the pressure coefficient along a line in the symmetry plane of the model showed that the general trend was correct in the simulation. However, in the separated region on the roof of the train model the negative pressure was underpredicted in the simulation compared to that in the experiments. This underprediction of the negative pressure in the separated region on the roof might be one reason to why the drag coefficient was predicted to 0.78 in the simulation compared to 0.86 in the experiments. This is because the separation starts already on the front edges and thus negative pressure on the curved edges contributes to a decrease in the over all drag coefficient of the train model. Adding four plates forming an open cavity on the aft on the train model proved to decrease the drag by some 10%. The primary mechanism by which the drag is decreased is that the plates effectively prevents the shear layers separating from the edges on the base of the train model from interacting to each other. This extends the size of the wake formed behind the train model and thereby the pressure inside the wake is increased and the decrease in the drag follows. It was found in the simulation that for the natural flow the wake extends approximately the distance of H behind the train model and with the attached cavity on the aft the wake extends 1.5 H. For higher Reynolds numbers, the reported experimental value of the drag coefficient is lower (≈ 0.4). This is because the flow does not separate from the leading edges in that case. This means that for higher Reynolds number, the placement of a cavity on the aft would lead to a higher relative decrease of the drag coefficient. This is in agreement with the results reported in i.e. [5] where a decreased drag coefficient of 23% was reported by placing a cavity on a ground vehicle bluff body without flow separation on the front of the vehicle model. The PANS $k-\epsilon-\zeta-f$ method has prevously been employed successfully to simulate the challenging unsteady flow around a landing gear [13]. The flow stayed attached on the front of the landing gear at the Reynolds number in that study. The present work shows that PANS is able to simulate the flow for a bluff body with separation from a curved surface at the front.

Acknowledgements

We are grateful to Dr. Yutaka Sakuma at RTRI for providing us with experimental data and geometrical details of the train model. This project is supported financially by Trafikverket (Swedish Transport Administration). Software licenses were provided by AVL List GMBH. Computations were performed at SNIC (Swedish National Infrastructure for Computing) at the Center for Scientific Computing at Chalmers (C3SE), Center for High Performance Computing at KTH (PDC) and National Supercomputer Center (NSC) at LiU.

References

[1] Sakuma, Y. and Ido, A. 2009 “Wind Tunnel Experiments on Reducing Separated Flow Region Around Front Ends of Vehicles on Meter-Gauge Railway Lines”. *Quarterly Report of RTRI*, Vol. 50, No. 1, pp. 20–25.

[2] Raghunathan, R. S., Kim, H.-D., and Setoguchi, T. 2002 “Aerodynamics of high-speed railway train”. *Progress in Aerospace Sciences*, Vol. 38, pp. 469–514.

[3] Orellano, A. and Sperling, S. 2009 “Aerodynamic Improvements and Associated Energy Demand Reduction of Trains”. *The Aerodynamics of Heavy Vehicles II: Trucks, Buses, and Trains*, vol. 41, pp. 219–231, Springer Berlin / Heidelberg.

[4] Khalighi, B., Zhang, S., Koromilas, C., Balkanyi, S. R., Bernal, L. P., Laccarino, G., and Moin, P. 2001 “Experimental and computational study of unsteady flow behind a Bluff Body with a drag reduction device”, SAE Paper 2001-01-1042.

[5] Verzicco, R., Fatica, M., Laccarino, G., and Moin, P. 2002 “Large Eddy Simulation of a road vehicle with drag-reduction devices”. *AIAA Journal*, Vol. 40, pp. 2447–2455.

[6] Coon, J. D. and Visser, K. 2004 “Drag Reduction of a Tractor-Trailer Using Planar Boat Tail Plates”. *The Aerodynamics of Heavy Vehicles: Trucks, Buses, and Trains*, vol. 1, Springer Berlin / Heidelberg.

[7] Grover, K. and Visser, K. D. 2001 “Over-the-road tests of sealed aft cavities on tractor trailers”, SAE Paper 2006-01-3529.

[8] Maeda, T. and Kondo, Y. 2001 “RTRI’s Large-scale Low-noise Wind Tunnel and Wind Tunnel Tests”. *Quarterly Report of RTRI*, Vol. 42, No. 2, pp. 65–70.

[9] Cooper, K. R. 1985 “The effect of Front-Edge Rounding and Rear Edge Shaping on the Aerodynamic Drag of Bluff Vehicles in Ground Proximity”, SAE Paper No. 850288.

[10] Girimaji, S. S. 2006 “Partially-Averaged Navier-Stokes Model for Turbulence: A Reynolds-Averaged Navier-Stokes to Direct Numerical Simulation Bridging Method”. *Journal of Applied Mechanics*, Vol. 73, pp. 413–421.

[11] Germano, M. 1992 “Turbulence: the filtering approach”. *Journal of Fluid Mechanics*, Vol. 238, pp. 325–336.

[12] Basara, B., Krajnović, S., S., G. S., and Pavlovic, Z. 2011 “Partially Averaged Navier-Stokes Method for Turbulence Simulations: Near-Wall Eddy Viscosity Transport Model Implementation”. *AIAA Journal*, Vol. in press, p. DOI: 10.2514/1.J050967.

[13] Krajnović, S., Lárusson, R., Helgason, E., and Basara, B. 2011 “PANS of Rudimentary Landing Gear”. *AIAA Paper AIAA-2011-3109. Nr. 153761*.

[14] Han, X., Krajnovic, S., and Basara, B. 2011 “Study of active flow control for a simplified vehicle model using PANS turbulence model”. *4th Symposium on Hybrid RANS-LES Methods*, September 28-30, Beijing China.

[15] Durbin, P. A. 1991 “Near-Wall Turbulence Closure Modeling Without Damping Functions”. *Theoretical and Computational Fluid Dynamics*, Vol. 3, pp. 1–13.

[16] AVL 2010 . CFD Solver. AVL Fire Manual, v2010.1, edition 11/2010.

[17] Patankar, S. and Spalding, D. 1972 “A calculation procedure for heat, mass and momentum transfer in three-dimensional parabolic flows”. *Int. J. Heat Mass Transfer*, Vol. 15, pp. 1787–1806.

[18] Krajnović, S. 2009 “LES of Flows Around Ground Vehicles and Other Bluff Bodies”. *Philosophical Transactions of the Royal Society A*, Vol. 367, No. 1899, pp. 2917–2930.

[19] Krajnović, S., Östh, J., and Basara, B. 2010 “LES Study of breakdown control of A-pillar vortex”. *Int. J. Flow control*, Vol. 2, No. 4, pp. 237–257.

[20] Krajnović, S., Östh, J., and Basara, B. 9-12 September, 2009 “LES of active flow control around an Ahmed body with Active Flow Control”. *Conference on Modelling Fluid Flow (CMFF’09), The 14th International Conference on Fluid Flow Technologies*, Budapest, Hungary.

[21] Östh, J. and Krajnović, S. 2012 “The flow around a simplified tractor-trailer model studied by Large Eddy Simulation”. *Journal of Wind Engineering and Industrial Aerodynamics*, Vol. 102, pp. 36–47.